Confidential: not for distribution. Submitted to the American Astronomical Society for peer review 2009 April 1

AMiBA 94 GHz SZE Observations: An Initial Measurement of H_0

Patrick M. Koch[1], Paul T. P. Ho[1,2], Chih-Wei Locutus Huang[3,4], Yu-Wei Liao[3,4], Kai-Yang Lin[1,3], Guo-Chin Liu[1,5], Sandor M. Molnar[1], Hiroaki Nishioka[1], Keiichi Umetsu[1,4], Fu-Cheng Wang[3,4], Jiun-Huei Proty Wu[3,4], Mark Birkinshaw[6], Katy Lancaster[6], Pablo Altamirano[1], Chia-Hao Chang[1], Shu-Hao Chang[1], Su-Wei Chang[1], Ming-Tang Chen[1], Chih-Chiang Han[1], Yau-De Huang[1], Yuh-Jing Hwang[1], Homin Jiang[1], Michael Kesteven[7], Derek Kubo[1], Chao-Te Li[1], Pierre Martin-Cocher[1], Peter Oshiro[1], Philippe Raffin[1], Ta-Shun Wei[1] & Warwick Wilson[7]

pmkoch@asiaa.sinica.edu.tw

ABSTRACT

Results on the Sunyaev-Zel'dovich effects (SZE) of a sample of six clusters of galaxies observed by the Yuan-Tseh Lee Array for Microwave Background Anisotropy (AMiBA) at 94 GHz in its 7-element configuration are combined with X-ray structure parameters to derive the cluster angular diameter distances and hence the Hubble constant, H_0. From the full cluster sample we find $H_0 = 50^{+16+17}_{-16-23}$ km s^{-1} Mpc^{-1} and $H_0 = 34^{+15+12}_{-15-15}$ km s^{-1} Mpc^{-1} for a cosmology with $(\Omega_M, \Omega_\Lambda) = (0.3, 0.7)$, assuming that the clusters are well described by isothermal β-models and 100 kpc cut models, respectively. The statistical errors are dominated by uncertainties in the cluster X-ray temperature and the SZE decrement. The systematic errors arise mostly from CMB structures and radio point sources. Possible corrections for asphericity, non-isothermality and radio point sources are discussed for the entire sample and subsamples. Excluding an obvious outlier, the isothermal β and the 100 kpc cut models yield values in close

[1]Academia Sinica, Institute of Astronomy and Astrophysics, P.O.Box 23-141, Taipei 10617, Taiwan

[2]Harvard-Smithsonian Center for Astrophysics, 60 Garden Street, Cambridge, MA 02138, USA

[3]Department of Physics, Institute of Astrophysics, & Center for Theoretical Sciences, National Taiwan University, Taipei 10617, Taiwan

[4]LeCosPa Center, National Taiwan University, Taipei 10617, Taiwan

[5]Department of Physics, Tamkang University, 251-37 Tamsui, Taipei County, Taiwan

[6]Department of Physics, University of Bristol, Tyndall Ave, Bristol, BS8 1TL, UK

[7]Australia Telescope National Facility, P.O.Box 76, Epping NSW 1710, Australia

agreement with $H_0 = 73 \pm 13\ \mathrm{km\,s^{-1}\,Mpc^{-1}}$ and $H_0 = 79 \pm 9\ \mathrm{km\,s^{-1}\,Mpc^{-1}}$ (random errors only), respectively. A comparison with the BIMA/OVRO results at 30 GHz shows the average ratio of the zero-frequency SZEs from AMiBA and BIMA/OVRO to be $s_{AB} = 1.27 \pm 0.14$ (100 kpc cut model) and $s_{AB} = 1.00 \pm 0.11$ (isothermal β-model), where the two cluster samples overlap, demonstrating the AMiBA consistency and feasibility at 94 GHz.

Subject headings: galaxy clusters: general — individual clusters, SZE observation, Hubble constant

1. Introduction

The hot X-ray emitting intracluster medium (ICM) scatters passing Cosmic Microwave Background (CMB) photons. On average, this inverse Compton scattering boosts the CMB photon energies, resulting in a small distortion ($\lesssim$1mK) of the original CMB spectrum. This is known as the Sunyaev-Zel'dovich effect (SZE) (Sunyaev & Zel'dovich 1972; Rephaeli 1995; Birkinshaw 1999). At frequencies below ~ 220 GHz the SZE decreases the brightness of the CMB, while at higher frequencies the CMB brightness is increased.

A combined analysis of SZE and X-ray data for a cluster of galaxies provides a method of measuring its distance, and hence the Hubble constant, H_0. This method of measuring H_0 was recognized by Cavaliere et al. (1977) and Silk & White (1978), and first applied by Birkinshaw (1979), and is based on the different scalings of the SZE and cluster X-ray brightness. The SZE produces a brightness temperature change proportional to the line-of-sight integrated electron pressure, $\Delta T_{SZ} \sim \int n_e T_e dl$, where n_e is the electron density, T_e is the ICM electron temperature, and dl is an element of length. The X-ray surface brightness, $S_X \sim \int n_e^2 \Lambda dl$, where Λ is the X-ray cooling function, is proportional to the line-of-sight integrated density squared. Adopting simplifying assumptions about the cluster (such as spherical geometry, no clumpiness), the cluster angular diameter distance can be found by eliminating a scale electron density to determine a cluster linear size, and then comparing this with the cluster angular size. This method relies on the comparison of line-of-sight and transverse sizes of the cluster, and so selection effects by surface brightness can be an issue. We note that this distance-measuring technique is independent of other methods for measuring H_0, and that it can be used to measure distances at high redshifts directly. A large sample of accurate SZE cluster distances extending to redshift one and beyond would allow the technique to be used to trace the expansion history of the Universe.

A growing literature reports SZE detections at various wavelengths with different instruments. Earlier observations were made with single dish telescopes at radio wavelengths (Birkinshaw & Hughes 1994; Herbig et al. 1995; Myers et al. 1997; Hughes & Birkinshaw 1998; Mason et al. 2001). Early results with bolometers (Holzapfel et al. 1997a,b; Lamarre et al. 1998; Komatsu et al. 1999; Pointecouteau et al. 2001) at millimeter wavelengths detected both the SZE decrement and increment, setting first limits to the cluster peculiar velocity. From initial low radio frequency observations with interferometers at an arcminute resolution scale (Jones et al. 1993; Grainge et al. 1993, 2002; Carlstrom et al. 1996, 2000; Grego et al. 2000, 2001) the cluster sample sizes have been continuously increased, (Reese et al. (2002): 18 clusters; Jones et al. (2005): 5 clusters; Bonamente et al. (2006); LaRoque et al. (2006): 38 clusters) making observations fairly routine now.

Deriving the Hubble constant from combined SZE and X-ray distance measurements provides a method independent from the approaches taken in supernova measurements (Riess et al. 2005), CMB cosmological parameter fitting (Spergel et al. 2003) or the *Hubble Space Telescope* key project (Freedman et al. 2001). For a complete discussion on the distance scale we refer the reader to Rowan-Robinson (1985).

In this paper we combine the first AMiBA cluster sample - all measured at 94 GHz - with published X-ray data to estimate H_0. The role of the paper is to demonstrate our instrument capabilities and its potential. In particular, we are exploring the science at 94 GHz, and we show the consistency with other SZE experiments at different frequencies. Focusing on the SZE measurement feasibility, we rely on published X-ray data for different cluster models. This paper completes a series of papers describing the AMiBA system performance and first science results. Joint AMiBA SZE data and Subaru weak lensing observations, combined with published X-ray temperatures are analyzed in Umetsu et al. (2009) in order to examine the distribution of total mass and gas. Huang et al. (2009) present AMiBA SZE - X-ray scaling relations. Future AMiBA observing capabilities for the upgraded system with 13 antennas of 1.2 m diameter are analyzed in Molnar et al. (2009).

The paper is organized as follows: Section 2 gives an overview of the AMiBA telescope. Section 3 describes in detail our initial cluster sample. The adopted cluster gas models and our analysis are given in section 4. The results for the angular diameter distance and Hubble constant are presented in section 5 together with the error analysis and possible model corrections. In section 6 we compare the AMiBA 94 GHz with the BIMA/OVRO 30 GHz results for those clusters where the two samples overlap. Our conclusions are given in section 7.

2. The 7-element AMiBA

AMiBA is a radio interferometer located at 3400 m at the Mauna Loa weather station on Big Island, Hawaii. It is designed for up to 19 elements with full polarization capabilities. AMiBA operates around 94 GHz (at a wavelength of about 3 mm) with a total bandwidth of about 16 GHz, split into an upper and lower sideband of about 8 GHz each. A 4-lag analog, broadband correlator outputs a set of 4 real-number correlation signals (Li et al. 2006; Chen et al. 2009). These four correlations are then transformed into 2 complex visibilities at the center frequencies of each frequency band (Wu et al. 2009). The AMiBA frequency band is chosen to take advantage of the optimal frequency window at 3 mm, where the SZE decrement is close to its maximum, and the contaminations by the Galactic synchrotron emission, dust foregrounds and radio point sources are minimized. In its first operation phase in 2007 and 2008, AMiBA operated with seven elements in a close-packed configuration with LL and RR correlations. The correlator and seven 0.6-m diameter Cassegrain antennas with receivers were mounted on a fully steerable 6-m diameter carbon-fibre platform, controlled by a novel hexapod mount. A series of companion papers gives a project overview (Ho et al. 2009) and describes in more detail the correlator and receiver (Chen et al. 2009), the antennas (Koch et al. 2006), and the hexapod mount (Koch et al. 2009).

The FWHM of the 0.6-m antennas is about $23'$ and the synthesized resolution in the initial, hexagonally close-packed, configuration (21 simultaneous baselines of 0.6 m, 1.04 m and 1.2 m) is about $6'$ with natural weighting. Although the antenna arrangement is reconfigurable with a maximum resolution of about $2'$ on the longest baselines ($\sim$5.6 m), the most compact configuration was chosen for initial AMiBA operations in order to maximize the short-spacing sensitivity. The heterodyne receivers — consisting of HEMT low-noise amplifiers (LNA) with $\sim$46 dB amplification, subharmonic mixers, and $2 - 18$ GHz IF amplifiers — have typical noise temperatures of $55 - 75$ K (Chen et al. 2009). The total system temperature, including CMB and contributions from the antenna, atmosphere and the ground, is $80 - 100$ K.

Typically, observations are carried out in a main-trail scheme. We estimate a point source sensitivity of about 63 mJy in a one-hour on-source integration (Lin et al. 2009) in this 2-patch differencing scheme. In this strategy, contaminating effects from ground pick-up and the hardware electronics (e.g. DC component) with variations on time scales longer than the switching scheme, can be successfully minimized in the data (Wu et al. 2009). Additionally, several platform polarizations (rotations around the optical pointing axis) are used in order to increase the *uv*-coverage and the imaging capabilities. While the broad-band correlator provides good sensitivity, having only four lags results in a relatively poorly measured bandpass response (band-smearing effect). This is corrected with the help of external calibrators (planets). Based on the measured system stability, calibration is done typically every 2 to 3 hours. This leads to an accuracy of $\sim \pm 5\%$ in gain and $\sim \pm$ 0.1 rad in phase for each baseline (Lin et al. 2009). About 10% of the telescope observing time is needed for calibration. The array overall efficiency is estimated to be $\sim$0.4, with the major losses coming from the antenna (antenna spill-over) and the noise from rejected correlations in the analog correlator (Lin et al. 2009).

With a center frequency around 94 GHz and possible baselines in a range of 0.6 to 5.6 m, AMiBA complements existing SZE/CMB instruments. Earlier interferometers were typically built for lower frequencies: AMI around 15 GHz (e.g., Kneissl et al. 2001; Zwart et al. 2008), BIMA/OVRO around 30 GHz (e.g., Myers et al. 1997; Reese et al. 2002; Bonamente et al. 2006; LaRoque et al. 2006), CBI around 31.5 GHz (e.g., Padin et al. 2000; Udomprasert et al. 2004), VSA around 33 GHz (e.g., Grainge et al. 2003; Lancaster et al. 2005). At these lower frequencies, significant effort has gone into studying the possible contamination of radio point sources in SZE observations. At higher frequencies, due to the negative spectral indices of most radio point sources, the contamination is expected to be significantly lower. We note that the SZA (Muchovej et al. 2007; Mroczkowski et al. 2008), with two frequency bands — 26-36 GHz and 80-115 GHz — and a wide range of baseline lengths is particularly powerful at reducing the point source confusion. It also provides complimentary information about smaller scale structures at AMiBA's operating frequency. Bolometer arrays at various frequencies — Diabolo at 140 and 250 GHz (Désert et al. 1998; Pointecouteau et al. 2001), SuZIE I,II,III at 145, 221 and 355 GHz (e.g.. Benson et al. 2004), APEX-SZ at 150 GHz (Dobbs et al. 2006; Halverson et al. 2008; Nord et al. 2009), ACT at 147, 215 and 279 GHz (Kosowsky 2003, 2006), SPT at 95, 150 and 225 GHz (Staniszewski et al. 2008) — provide complimentary high-sensitivity observations.

3. Initial cluster sample

As initial targets we chose six massive Abell clusters, at redshifts 0.09 - 0.32, which have been reported to be strong SZE sources (Table 1). These were observed over about 40 nights from April to August 2007. Four of the clusters overlap with the BIMA/OVRO samples (Reese et al. (2002), 18 clusters; Bonamente et al. (2006), 38 clusters). Having different frequencies and resolutions (94 GHz and $\sim 6'$ for AMiBA, 30 GHz and $\sim 1'$ or less for BIMA/OVRO) our observations are complimentary, but subject to similar biases. We will address this in the sections 4 and 5. These six clusters have sufficiently high X-ray total flux densities that the surface brightness selection bias should not be an issue.

Our observing strategy, calibration scheme and data analysis methods are described in detail in Lin et al. (2009); Wu et al. (2009); Nishioka et al. (2009).

3.1. A1689

Our total on-source integration time for A1689 ($z = 0.183$) is about 12 hours, giving an S/N ratio of about 7.6. Abell 1689 is a cluster showing large discrepancies (of a factor of two or more) among various mass determinations. It is a cluster without a pronounced cooling flow. Optical data indicate that it consists of substructures and so is not fully relaxed. Miralda-Escudé & Babul (1995) suggest a strong lensing model consisting of two clumps in order to reproduce the position of the brightest arcs. The derived X-ray virial mass is about a factor of two lower than the gravitational lensing mass. Girardi et al. (1997) also identify two substructures based on redshift data. Their virial mass is several times lower than the mass derived from lensing. More recently, a lower X-ray virial mass has been found from *XMM-Newton* observations (Andersson & Madejski 2004). The derived gas mass fraction $f_{gas} = M_{gas}/M_{tot} = 0.07 \pm 0.01$ is significantly smaller than $f_{gas} = 0.108 \pm 0.014$ from Allen et al. (2003) for 10 dynamically relaxed clusters. Andersson & Madejski (2004) also find an asymmetric temperature distribution which provides further evidence that the cluster is not in a relaxed state. Contrary to this, Chandra observations show an overall symmetric morphology of the X-ray surface brightness and a nearly constant temperature across the cluster surface out to $r \sim 1$ Mpc (Xue & Wu 2002). This suggests that A1689 is dynamically relaxed. Whereas the mass (based on a double β-model) within the central 0.2 Mpc is again systematically lower than the value derived from strong and weak-lensing techniques, at large radii r >0.6 Mpc the two estimates yield roughly the same mass. The central cD galaxy coincides with the X-ray peak which further supports the hydrostatic equilibrium assumption (Lemze et al. 2008). It also coincides with the center of mass derived from strong lensing in Lemze et al. (2008). A1689 has the largest Einstein radius known to date (53" for a source at z=3). Recent careful lensing studies show that the form of lensing profiles of A1689 is consistent with a continuously steepening density profile, well described by the general NFW model (Navarro et al. 1997). Its projected mass profile, however, is highly centrally concentrated with the degree of concentration, $c_{\rm vir} > 10$ (Broadhurst et al. 2005; Limousin et al. 2007; Umetsu & Broadhurst 2008; Corless et al. 2009; Umetsu et al. 2009), lying well beyond the ΛCDM prediction ($c_{\rm vir} \sim 4$; see, e.g., Duffy et al. (2008)) for a high-mass cluster of $M_{\rm vir} \sim 1.5 \times 10^{15} h^{-1} {\rm M}_{\odot}$ ($h = 0.719$). Recently, a good consistency of the lensing results was obtained with detailed multi-wavelength studies including Chandra X-ray observations (Lemze et al. 2008) and VLT/VIMOS dynamical observations (Lemze et al. 2009).

The SZE in A1689 has been measured with several instruments: BIMA/OVRO at the

SZE decrement (Grego et al. 2001; Reese et al. 2002; LaRoque et al. 2006), with SuZIE and SCUBA at the SZE increment. Limits to its peculiar velocity were set in Holzapfel et al. (1997a) with $v_r = 170^{+815}_{-630}$ km s^{-1} from a simultaneous fit from the SuZIE 2.1 mm and 1.4 mm band observations. Updated numbers based on a isothermal β-model integrated SZE flux are presented in Benson et al. (2004) from SuZIE II measurements. A1689 is also one of the clusters used in the stacked deep integration fields of SCUBA at 850 μm in order to constrain a cluster profile (Zemcov et al. 2007). Two radio point sources of about 0.5 mJy and 1.3 mJy at 1 cm are present in this cluster. Combined with lower frequency observations, a spectral index of -1.4 and -1.1 is derived (Cooray et al. 1998).

3.2. A1995

In a total integration time of about 5.5 hours, A1995 ($z = 0.322$) was detected with AMiBA with a signal to noise ratio of about 6. In the *ROSAT* All-Sky-Survey (Briel & Henry 1993) the cluster is listed with an X-ray luminosity $L_X = 8.67 \times 10^{44}\, h_{50}^{-2}$ ergs s^{-1} in the 0.5-2.5 keV cluster rest frame energy band. Its temperature measured from *ASCA* spectra is $10.7^{+2.5}_{-1.8}$ keV (Mushotzky & Scharf 1997). A later broad-band (1-9 keV) single phase plasma fit from deconvolved *ASCA* data yielded $T = 7.57^{+1.07}_{-0.76}$ keV and $Z = 0.21^{+0.15}_{-0.15}$ solar abundance. Due to the cluster's small angular size, temperature and abundance profiles are not resolved in these data (White 2000). Baldi et al. (2007) analyzed A1995 in a *Chandra* archival study. The temperature profile is found to be flat within errors, with a temperature around 9 keV. The abundance profile shows a tendency to increase at the outer radii. Weak lensing studies (Dahle et al. 2002) show an elongated light distribution in the northeast-southwest direction, whereas the mass distribution is circularly symmetric which is consistent with the *ROSAT* HRI image in Patel et al. (2000).

The only SZE observations to date are from the BIMA/OVRO array around 30 GHz (Patel et al. 2000; Reese et al. 2002; LaRoque et al. 2006; Bonamente et al. 2006). X-ray, optical and SZE data were combined in Patel et al. (2000) in order to derive the cluster gas mass, total virial mass, its angular distance and a Hubble constant $H_0 \approx 52$ km s^{-1} Mpc^{-1}. A1995 appears to be relatively free of radio point source contamination, with only two sources. These have flux densities of less than 10 mJy at 20 cm and less than 1 mJy at 1 cm (Cooray et al. 1998).

3.3. A2142

We observed A2142 ($z = 0.0899$) over eight nights in April and May 2007. Serving as our first and brightest SZE cluster, we also tried center offset and a 3-patch (lead-main-trail) observations. The on-source integration time used for the present analysis was about 6 hours, giving an S/N ratio of almost 14.

A2142 is listed as a cooling flow cluster with a cooling flow rate of about 300 $M_{\odot}yr^{-1}$ (Peres et al. 1998). This hot ($\sim 9\,$keV) X-ray luminous cluster has two bright elliptical galaxies near the center which are aligned in the direction of the X-ray brightness elongation. The cluster is probably not in a dynamically relaxed state since the line-of-sight velocities of these galaxies differ by about 1800 km s^{-1} (Oegerle et al. 1995). The Chandra X-ray observations (Markevitch et al. 2000) further support a scenario of a late-stage unequal mass merger based on two sharp brightness edges which are likely the dense ram pressure-stripped subcluster cores. In this process the central cooling flow has been disturbed and the central cluster region is markedly non-isothermal with temperatures ranging from 5 to more than 12 keV. Ettori & Fabian (2000) later used this sharp temperature gradient to constrain the cluster plasma conductivity. A highly irregular mass distribution supporting the merger scenario was also found in the weak lensing maps by Okabe & Umetsu (2007).

A2142 was observed by VSA (Lancaster et al. 2005) where the SZE was detected relatively free from CMB contamination. Seven radio point sources (with a predicted flux density at 34 GHz up to 500 mJy) are included in the model of the sky. Myers et al. (1997) observed A2142 with the OVRO telescope at 32 GHz with a bandwidth of 6.5 GHz. Flux densities for four radio point sources within $9'$ of the field center (Myers et al. 1997) and later within $12'$ (Mason et al. 2001) were extrapolated based on the 1987 Green Banks survey at 4.85 GHz (Gregory & Condon 1991) and OVRO 40 m follow-up observations at 18.5 GHz. For each source the spectral index α, assuming a power-law spectrum $S \sim \nu^{\alpha}$, was found to be negative.

3.4. A2163

We observed A2163 ($z = 0.2030$) during 3 nights in May 2007 with a total on-source integration time of about 7.5 hours, which yielded a signal to noise ratio close to 12. A2163 is among the hottest and most X-ray luminous clusters known (Arnaud et al. 1992). An extended radio halo was first reported by Herbig & Birkinshaw (1994). *Chandra* temperature maps (Markevitch & Vikhlinin 2001; Govoni et al. 2004) show that the cluster is a merger exhibiting a distorted X-ray morphology with strong gas temperature variations of at least a factor of two. The X-ray image (Govoni et al. 2004) shows streams of hot and cold gas together with a possible remnant of a cool gas core. The merger is likely to occur at a large angle to the plane of the sky. High-temperature regions seem to be spatially correlated with diffuse radio emission. This confirms the interpretation that radio halos are related to cluster mergers, supporting a merger shock origin for the relativistic halo electrons. The *XMM-Newton* mosaic observation (Pratt et al. 2001) shows a flat radial temperature profile out to about half the virial radius followed by a slight decline. The VLA radio spectral index maps (Feretti et al. 2004) at 0.3 GHz and 1.4 GHz reveal patches of different spectral index values which is interpreted as evidence for a complex shape of the electron spectrum as it is expected in a particle re-acceleration scenario. A radio relic is identified in the NE peripheral cluster region (Feretti et al. 2001). Observations by the *RXTE* satellite (Rephaeli et al. 2006) reveal a 25% non-thermal emission in the integrated $3-50\,\mathrm{keV}$ band, likely to origin from the central prominent extended radio halo. From this result (assuming a radio emitting relativistic electron population) a volume-averaged magnetic field $B = 0.4 \pm 0.2\,\mu\mathrm{G}$ is derived.

A detailed complementary optical study to constrain the merger dynamics was undertaken by Maurogordata et al. (2007). From 512 objects, 361 were identified as cluster members with two dominant substructures: a main central component with a recent merger and a northern component which is likely infalling. The velocity distribution shows multi-modality with a large velocity gradient in the NE-SW direction, which is likely to be the merger axis. From 326 high-precision redshift measurements the mean cluster redshift is derived to be $z = 0.2005 \pm 0.0003$. The combined optical and X-ray data leads to an exceptionally massive cluster of $M = (3.8 \pm 0.4) \times 10^{15}\,\mathrm{M}_{\odot} h_{70}^{-1}$.

SZE observations toward A2163 have been carried out in the three SuZIE spectral bands (1.1mm, 1.4mm, 2.1mm) in order to set limits on the cluster peculiar velocity v_r (Holzapfel et al. 1997a). They find $v_r = 490^{+1370}_{-880}\,\mathrm{km\ s^{-1}}$. The radio point source flux density is estimated to be less than 1 mJy, based on measured spectral indices. One radio point source is reported to be time variable. LaRoque et al. (2002) derived an SZE spectrum combining the SuZIE bands and the BIMA/OVRO interferometric detection. Radio point sources were identified from high-resolution maps from baselines 20 m and longer, and then jointly fit with the SZE decrement. Recently, APEX-SZ (150 GHz) and LABOCA (345 GHz) results from an isothermal β-model have been additionally added to derive $v_r = -140 \pm 460\,\mathrm{km\ s^{-1}}$ (Nord et al. 2009).

A2163 has also been used as a testbed for the non-thermal SZE (Colafrancesco et al. 2003) and as a probe to test the CMB temperature evolution as a function of redshift together with the Coma cluster (Battistelli et al. 2002).

3.5. A2261

During 4 nights with about 9 hours on-source integration, A2261 was detected with AMiBA with a signal to noise ratio of about 5. A2261 is a moderate redshift cluster ($z = 0.224$) in the *ROSAT* Brightest Cluster Sample (BCS, Ebeling et al. (1998)) with a temperature of $\sim$10.8 keV and $L_X \approx 18.2 \times 10^{44}\, h_{50}^{-2}$ erg s^{-1} in the 0.1-2.4 keV range. In this sample, A2261 is classified as a cool core cluster with a regular morphology (Bauer et al. 2005) with some evidence of mild substructure, perhaps indicative of recent minor merger activities. A2261 was also used in a recent *Chandra* archival study of temperature and metal abundance profiles by Baldi et al. (2007). A global temperature of $< kT >= 7.43^{+0.49}_{-0.27}$ keV and a global metallicity of $< Z >= 0.30^{+0.07}_{-0.06}$ were derived. The temperature profile shows a hint of a decrease in the center, dropping from 9.0 ± 0.4 to 7.7 ± 0.4 keV. The metallicity profile appears to be constant, decreasing only in the outer radial bin. Weak lensing observations (Dahle et al. 2002) show a circularly symmetric light distribution, where the center is dominated by a bright cD galaxy. The mass and number density distributions are more elongated, with the mass peak being offset by $\approx 1'$ from the light peak. A strong lensing arc southwest of the cD galaxy is detected both by Dahle et al. (2002) and by Sand et al. (2005) in *HST* images.

The SZE in A2261 has been measured at the decrement (Grego et al. 2000; Reese et al. 2002), around the null (Benson et al. 2003), and close to the maximum increment with SCUBA at 850 μm (Zemcov et al. 2007). Simultaneous multi-frequency measurements with SuZIE II at 3 frequencies (145, 221, 355 GHz) have been used in order to separate the kinematic and thermal SZE, leading to a peculiar velocity of -1575^{+1500}_{-975} km s^{-1} (Benson et al. 2003). SCUBA observations at 850 μm (Chapman et al. 2002) revealed a point source of 17.6 ± 3.9 mJy, leading to a systematic bias in the peculiar velocity of several hundred kilometers per second towards negative values. At lower frequencies, no radio point sources are detected within $1'$ of the brightest central galaxy (Gregory & Condon 1991; White & Becker 1992; Crawford et al. 1995). At a distance of more than $2'$ from the center, a point source with a flux density of 3.88 ± 0.88 mJy at 1 cm is found from OVRO observations (Cooray et al. 1998). A negative spectral index is derived in combination with 20 cm data.

3.6. A2390

A2390 ($z = 0.228$) was observed with a total on-source integration time of 11 hours and detected with a S/N ratio of 6.6. This cluster has a high X-ray luminosity ($L_X = 2.1 \times 10^{45}\, h_{50}^{-2}\, \mathrm{erg\, s^{-1}}$, $0.1 - 2.4\, \mathrm{keV}$, Ebeling et al. (1996)). From recent *Chandra* observations (Allen et al. 2001) it is known to have a cooling flow ($\lesssim 300\, \mathrm{M_\odot\, yr^{-1}}$). The temperature of the X-ray gas rises with increasing radius within the central $\sim 200\,\mathrm{kpc}$ of the cluster, and then approximately remains isothermal, with kT = $11.5^{+1.5}_{-1.6}\,\mathrm{keV}$ out to $\sim 1\,\mathrm{Mpc}$. This is in agreement with previous results of kT = $14.5^{+5.5}_{-5.2}\,\mathrm{keV}$ from Allen (1998) based on ASCA observation, and kT = $11.1^{+1.5}_{-1.6}\,\mathrm{keV}$ from Böhringer et al. (1998) based on a joint analysis of *ASCA* and *ROSAT* PSPC data. These earlier measurements yielded higher cooling flow mass deposition rates. The X-ray morphology is elongated along an approximately northwest-southeast direction, similar to the optical luminosity distribution and lensing mass models of Pierre et al. (1996). The *Chandra* image also shows substructure, suggesting that the cluster has not yet fully relaxed after the most recent merger. However, X-ray and gravitational lensing mass measurements (Squires et al. 1996; Pierre et al. 1996) show a mean scatter of less than 20% within the central 1 Mpc region (Allen et al. 2001), which suggests that the hydrostatic equilibrium assumption is reasonable. A kpc-scale radio structure associated with the cD galaxy has been found from VLA, VLBA and Merlin observations (Augusto et al. 1998, 2006). The radio source shows a flat spectrum up to $\sim 40\,\mathrm{GHz}$ ($S_\nu \sim 100\,\mathrm{mJy}$), with a twin-jet structure and expanding bubbles possibly blown into the ICM.

Multi-frequency observations in order to fit the SZE spectral function have been conducted with SuZIE II at the 145, 221 and 355 GHz bands towards 11 clusters including A2261 and A2390 (Benson et al. 2003, 2004). A spherical symmetric β-model has been adopted to calculate the integrated SZE flux density, which is argued to be a more robust observable than the central Comptonization. The SuZIE central Comptonization values are up to 60% and 12% higher than BIMA/OVRO interferometric values for cooling flow and non-cooling flow clusters. High frequency SZE signals have been obtained with SCUBA at 850 μm, close to the maximum SZE increment (Zemcov et al. 2007). A2390 (together with A1689, A2163, A2261 from our sample) is among their sample of 44 clusters. 17 deep integration fields (free of radio source contamination) are stacked in order to derive and discuss radial averages of the SZ decrement. The peak increment value is detected at 9σ.

4. Cluster Gas Models and Analysis

4.1. Cluster Density Models

Due to the current limited *uv*-plane coverage and resolution of AMiBA in its 7-element compact configuration, the structures of the clusters are based on X-ray data alone. The central SZE surface brightnesses of the clusters are then fitted from the X-ray based models (Liu et al. 2009). Aiming again at demonstrating the feasibility and consistency of our results at 94 GHz, we are probing a selection of cluster gas models used for previous SZE observations at lower frequencies.

The isothermal spherical β-model (Cavaliere & Fusco-Femiano 1976) is commonly used for cluster X-ray and SZE analysis. The electron number density n_e as a function of the cluster radius r is given as

$$n_e(r) = n_{e0}\left(1 + \frac{r^2}{r_c^2}\right)^{-3\beta/2}, \tag{1}$$

where r_c, β and n_{e0} are the cluster core radius, a structure parameter and the central electron number density. Conveniently, the spherical isothermal β-model allows for simple analytical expressions for the X-ray and SZE surface brightnesses:

$$S_X = S_{X0}\left(1 + \frac{\theta^2}{\theta_c^2}\right)^{(1-6\beta)/2}, \tag{2}$$

$$\Delta T = \Delta T_0\left(1 + \frac{\theta^2}{\theta_c^2}\right)^{(1-3\beta)/2}, \tag{3}$$

where S_{X0} and ΔT_0 are the central X-ray surface brightness and the central SZE temperature decrement/increment, respectively. θ_c is the cluster core angular size.

In the most recent and currently most extended cluster studies based on *Chandra* X-ray and BIMA/OVRO SZE data, results of H_0 (Bonamente et al. 2006) and the gas mass fraction f_{gas} (LaRoque et al. 2006) were compared for cluster gas models of increasing complexity. In the most sophisticated cluster plasma model, a double β-model for the gas density is combined with a temperature profile, assuming that the ICM is in hydrostatic equilibrium with a NFW dark matter density distribution (Navarro et al. 1997). This model particularly assesses the bias from the isothermal gas assumption. Additionally, with two β-model components, the narrow, peaked central density and the outer shallower cluster profile can be fitted. In this way the central sharp X-ray emission is more accurately modeled.

In order to exclude the cooling regions in cool-core clusters, Bonamente et al. (2006) and LaRoque et al. (2006) also examined a single isothermal β-model where the central 100 kpc is removed for the X-ray analysis. As the authors remark, the 100 kpc region is large enough to exclude the cooling region but still leaves sufficient X-ray photons for the modeling. They find that the X-ray surface profiles are then well described by the isothermal β-model beyond 100 kpc from the cluster center. A possible systematic bias from cool-core clusters is minimized with this 100 kpc cut model. LaRoque et al. (2006) also demonstrate the importance of proper treatment of the cluster core in the case of cool-core clusters. Striking differences are found in the masses derived from a simple isothermal β-model versus those from the two models described above. On the other hand, for non-cool-core clusters the results are largely insensitive to the chosen model. In particular, the simpler 100 kpc cut model works equally well as the more complicated non-isothermal double β-model.

Additionally, LaRoque et al. (2006) also tested an SZE-only model. Since their SZE spatial data do not have sufficient spatial dynamic range, β was fixed to a sample mean value in order to constrain θ_c. In Bonamente et al. (2006) a simple isothermal β-model is also compared to the 100 kpc cut model and the non-isothermal double β-model when deriving H_0. Comparing all three models, they find a spread in H_0 of only $3\,\mathrm{km\,s^{-1}\,Mpc^{-1}}$, which indicates that the distance scale from their 38 cluster sample is rather insensitive to the detailed ICM modeling. Similarly, for the same sample, LaRoque et al. (2006) find that the isothermal β-model characterizes well the ICM outside the cluster core for clusters with a range of different morphologies. Cluster cores can be satisfactorily modeled by either excluding them from fits to X-ray data or modeling the total ICM with a non-thermal double β-model. It needs to be stressed that this is for X-ray data, the current SZE data are largely insensitive to core structures.

At least 4 clusters of our initial sample are cooling flow clusters (Table 1). We therefore adopt a 100 kpc cut model in order to account for a possible bias from a cool-core. For comparison we also provide results for an isothermal spherical β-model.

4.1.1. 100 kpc cut model

The cluster X-ray parameters based on *Chandra* data are summarized in Table 2. Except for A2142 and A2390, we adopt the values from Bonamente et al. (2006) from their Table 4. A β-model is fitted to the data with the central 100 kpc excised. The cluster central value S_{X0} is then obtained by extrapolation. Their cooling functions are from a Raymond-Smith spectral emissivity code. The cooling function is red-shifted to the detector frame, convolved with the telescope response and integrated over the 0.7-7 keV *Chandra* bandpass. Allen et al. (2001) analyzed A2390 and fit the azimuthally averaged surface brightness profile with different models. Besides a broken power-law model, an 80 kpc cut model improves the simple β-model fit and accounts for the central cooling region. We derive S_{X0} from extrapolating their value at 80 kpc. A sample averaged cooling function is assumed. Here, we exclude A2142 from the sample due to its obvious bimodal structure in the high-resolution *Chandra* image (Markevitch et al. 2000).

LaRoque et al. (2006) and Bonamente et al. (2006) already remark that there is no simple way to remove the central 100 kpc from the SZE data because the analysis is done in the uv-plane. However, since the SZE probes the integrated gas pressure (and is linear in density n_e) it is less sensitive to the denser cluster cores than the X-ray surface brightness ($\propto n_e^2$). This is the case provided that the gas flows in the cluster are sufficiently subsonic so that the pressure is not affected by changes in the temperature alone. Generally, in a joint

SZE/X-ray analysis, the SZE also has little effect on the shape parameters θ_c and β, because they are mainly driven by the X-ray data. Moreover, AMiBA in its initial configuration, is only sensitive to the cluster largest scales since it marginally resolves their SZEs and is relatively insensitive to changing pressures in the cluster cores. Our SZE data, therefore, only constrain the overall normalization of the SZE signal. We thus fit the entire SZE data set in the uv-plane by holding the 100 kpc cut model parameters from X-rays fixed (Liu et al. 2009) (Table 2).

4.1.2. Spherical Isothermal β-model

For consistency with earlier work, (e.g. Birkinshaw et al. (1991); Holzapfel et al. (1997a); Hughes & Birkinshaw (1998); Mason et al. (2001); Reese et al. (2002); Schmidt et al. (2004); Udomprasert et al. (2004); Muchovej et al. (2007)) we also test the spherical isothermal β-model for cluster atmospheres. Biases introduced by this simple model are discussed in section 5.2. The cluster X-ray parameters are summarized in Table 3, which are based on *ROSAT* PSPC structural fits and *ROSAT* or *ASCA* temperatures assuming the cluster atmospheres to be isothermal. Estimates of the central spectral emissivity Λ_{eH0} for A2142 and A2390 were estimated for an observed X-ray band of $0.5-2$ keV (as in Reese et al. (2002)) and 0.3 solar abundance, assumptions that reproduce the Λ_{eH0} values from Reese et al. (2002) to better than $\sim 1\%$. Our central SZE values ΔI_0 were again derived from a maximum likelihood analysis in the uv-plane by holding the X-ray parameters fixed (Liu et al. 2009). Table 3 lists the measured values without contamination estimation from CMB and radio point sources.

4.2. Analysis

For both the 100 kpc cut and the isothermal β-model we calculate the angular diameter distance using the X-ray surface brightness and the zero-frequency SZE (e.g. Reese et al. (2002); Molnar et al. (2002)) as

$$
\begin{aligned}
D_A = \quad & \left(\frac{(\Delta T_0)^2}{S_{X0}}\right)\left(\frac{m_e c^2}{kT_e}\right)^2 \frac{\Lambda_{eH0}\,(\mu_e/\mu_H)}{4\pi^{3/2}T_{CMB}^2 f(x,T_e)^2\sigma_T^2(1+z)^4}\frac{1}{\theta_c} \\
& \times\left[\frac{\Gamma(3\beta/2)}{\Gamma(3\beta/2-1/2)}\right]^2\frac{\Gamma(3\beta-1/2)}{\Gamma(3\beta)} \quad . \qquad (4)
\end{aligned}
$$

Here T_{CMB} is the CMB temperature, z is the cluster redshift, T_e is the electron temperature, and k, m_e, c and σ_T are the Boltzmann constant, the electron mass, the speed of light and the Thomson cross section, respectively. $f(x, T_e)$ is the SZE thermal spectrum for the brightness temperature, expressed in terms of the dimensionless frequency $x = \frac{h\nu}{kT_{CMB}}$ and taking account of the $5-8\%$ relativistic corrections at 94 GHz for these clusters (Challinor & Lasenby 1998; Itoh et al. 1998; Nozawa et al. 2000). $\Gamma(x)$ is the gamma function. For the X-ray parameters (S_{X0}, β, θ_c, T_e) and ΔT_0 either the 100 kpc cut model values (Table 2) or the isothermal β-model values (Table 3) are adopted. $\Lambda_{eH0}\,(\mu_e/\mu_H)$ is replaced by Λ_{ee} in the case of the 100 kpc cut model. The values of the central SZE temperature decrement ΔT_0 were calculated from the central SZE brightness changes measured by AMiBA using

$$\Delta I_0 = \frac{2\nu^2 kT_{CMB}}{c^2}\frac{x^2 e^x}{(e^x-1)^2}\frac{\Delta T_0}{T_{CMB}}, \tag{5}$$

and are given in the Tables 2 and 3 for the 100 kpc cut model and the isothermal β-model, respectively.

The Hubble constant H_0 as a function of the cosmological model is then derived from (e.g., Carroll, Press & Turner 1992)

$$\frac{1}{c}H_0 D_A(z) = \frac{1}{1+z}\begin{cases} \frac{1}{|\Omega_k|^{1/2}}\sinh\{\Omega_k^{1/2}\,\mathcal{E}(z)\} & \Omega_k > 1, \\ \mathcal{E}(z) & \Omega_k = 0, \\ \frac{1}{|\Omega_k|^{1/2}}\sin\{|\Omega_k|^{1/2}\,\mathcal{E}(z)\} & \Omega_k < 1, \end{cases} \tag{6}$$

where $\mathcal{E}(z) = \int_0^z [(1+\tilde{z})^2(1+\Omega_M\tilde{z}) - \tilde{z}(2+\tilde{z})\Omega_\Lambda]^{-1/2}d\tilde{z}$. Ω_M, Ω_Λ and $\Omega_k = 1-\Omega_M-\Omega_\Lambda$ are the fractional contributions of matter, the cosmological constant Λ and curvature at the present epoch, respectively.

5. Results

5.1. D_A and H_0

The angular diameter distances D_A for our cluster sample are listed in the Tables 4 and 5 for the 100 kpc cut and the isothermal β-model, respectively, where the observational uncertainty budget is broken down into its components. Originally asymmetric error bars have been symmetrized and propagated with a Monte-Carlo simulation (100,000 realizations). All errors are 1σ uncertainties. The errors in Λ_{eH0} and Λ_{ee} are small ($\sim 1-2\%$), and so are neglected. Similarly, the error in the values of μ_H/μ_e are negligibly small. Based on these D_A estimates we fit values of H_0 as given in Table 6, based on the the full cluster sample, different cluster subsamples, and with variations from the original models (100 kpc cut or isothermal β), as discussed further below.

Angular diameter distances derived from the 100 kpc cut model and the isothermal β-model are compared in Fig. 1. Model corrections are illustrated in Fig. 2 for the isothermal β-model, as listed in Table 5. Similar corrections for cluster asphericity and point sources apply to the 100 kpc cut model (Table 4), but are not separately shown here.

5.2. Systematic Errors

The bias from the possible selection effect of choosing the brightest SZE clusters is likely to be small for this sample since it was based on the strong X-ray clusters. We then estimate possible systematic errors from two main sources: shortcomings in the cluster modeling and remaining instrumental uncertainties. Various aspects of cluster atmospheres and morphologies have been addressed in the literature. A random uncertainty of about $\pm 20\%$ in H_0 is expected from asphericity for one cluster (Hughes & Birkinshaw 1998). This leaves our sample with a $\pm 20/\sqrt{6} \approx \pm 8\%$ and $\pm 20/\sqrt{5} \approx \pm 9\%$ uncertainty for the isothermal β and the 100 kpc cut model, respectively, with a possible bias from the selection for significant SZEs. For a general isothermal spherical cluster model, Kawahara et al. (2007) have identified three main systematic errors from both analytic and numeric modeling: inhomogeneities in the ICM, departure from isothermality and the difference between the X-ray spectroscopic T_{spec} and emission-weighted temperature T_{ew} in the ICM. Fluctuations in the gas density overestimate H_0 by $\sim 30\%$. We adopt this estimate for the isothermal β-model and also for the 100 kpc cut model, because even the highest resolution *Chandra* observations do not yet resolve these density fluctuations. Temperature fluctuations are not significant. H_0 is underestimated by $\sim 10 - 20\%$ if the real temperature follows a polytropic profile instead of $T_{spec} = const$. We use this estimate for the isothermal β- model. We assume this error to be negligible for the 100 kpc cut model, where the cluster center is excised to leave an almost constant temperature profile for the cluster outer region. Using T_{ew}, which is systematically larger than T_{spec}, would result in another $\sim 10\%$ underestimation of H_0. Taking into account an ellipsoidal shape, Kawahara et al. (2007) find an average bias of $\sim 15\%$, which applies again for both of our spherical models, independent of the *ROSAT* or *Chandra* resolution.

Clusters move with respect to the CMB frame with a rms relative velocity of $\sim 300\,\mathrm{km\,s^{-1}}$ (Colberg et al. 2000). This kinetic SZE component leads to an under- or overestimated thermal SZE. At the AMiBA observing frequency this is $\sim \pm 3\%$ of the thermal SZE component for a 10-keV cluster, and hence produces a $\sim \pm 6\%$ uncertainty for an individual cluster D_A for both the isothermal β and the 100 kpc cut model. Contaminations from CMB and undetected radio point sources are estimated based on sample averaged ΔI_0 uncertainties from Liu et al. (2009) and are similar for both tested models. Finally, the AMiBA SZE absolute calibration yields an uncertainty of about ±10%, with $\sim \pm 5\%$ systematic and $\sim \pm 5\%$ statistical errors (Lin et al. 2009). Including all systematic errors (Table 7), we derive $H_0 = 50^{+16+17}_{-16-23}$km s^{-1}Mpc^{-1} and $H_0 = 34^{+15+12}_{-15-15}$km s^{-1}Mpc^{-1} for the isothermal spherical β-model and the 100 kpc cut model, respectively, where the errors are observational followed by systematic 1σ values.

All the results are quoted including relativistic corrections. Using the non-relativistic formula for the SZE, the values of D_A in the Tables 4 and 5 would be lower by about 10 % in each cluster.

5.3. Model corrections

Here we attempt to correct the individual cluster D_A for three model-dependent systematic errors. De Filippis et al. (2005) reconstructed the three-dimensional cluster morphology assuming triaxial ellipsoids with one principal axis along the line of sight. Their sample includes five of our clusters for which they give a projected axial ratio e_{proj}. Whereas the spherical central X-ray surface brightness and β remain practically unchanged by the elliptical β fit, the projected core radius is corrected (to first order) by a factor $2e_{proj}/(1+e_{proj})$. Table 4 and 5 show the morphology-corrected D_A^{ell} based on the corrected radius values for the 100 kpc cut and the isothermal β-model. The aphericity correction is illustrated for the spherical β-model in Figure 2. For both models this morphology correction increases the estimate for H_0 (Table 6).

Corrections based on individual cluster temperature structures are not well known. To estimate the likely sizes of these corrections we extend the cluster gas model by adopting a polytropic profile of index γ, so that $T_e(r) = T_{e0}(n_e(r)/n_{e0})^{\gamma-1}$. We apply this correction only to the isothermal β-model, because the non-isothermality bias is supposed to be significantly reduced in the 100 kpc cut model. This alters equation (4) mostly by modifying the gamma functions, with $\beta \rightarrow \beta\gamma$ in those in the square brackets, and $\beta \rightarrow \beta(\gamma/4 + 3/4)$ in the final ratio (Puy et al. 2000):

$$\begin{aligned} D_A^T = \quad & \left(\frac{(\Delta T_0)^2}{S_{X0}}\right)\left(\frac{m_e c^2}{kT_{e0}}\right)^2 \frac{\Lambda_{eH0}\,(\mu_e/\mu_H)}{4\pi^{3/2}T_{CMB}^2 f(x)^2\sigma_T^2(1+z)^4}\frac{1}{\theta_c} \\ & \times\left[\frac{\Gamma(3\beta\gamma/2)}{\Gamma(3\beta\gamma/2-1/2)}\right]^2 \frac{\Gamma(3\beta(\gamma/4+3/4)-1/2)}{\Gamma(3\beta(\gamma/4+3/4))}. \end{aligned} \tag{7}$$

We note that this approximation is possible because Λ_{eH} is relatively sufficiently weak function of temperature in the ROSAT band. For the same reason, we would not expect the values of T_{e0} to change significantly, and so we can assess the effect of a non-isothermal model by adopting the values of $(T_{e0}, \theta_c, \beta)$ given in Table 3. The effect of changing from an isothermal ($\gamma = 1$) model to $\gamma \in [1.1, 1.3]$, to produce new angular diameter distance estimates D_A^T, is shown in Table 5 and Figure 2. It appears that large values of γ are inconsistent with the current consensus range for H_0.

We correct for radio point source contamination following the method described in Liu et al. (2009). Significant contamination from discrete radio sources (at a level of 3-60 %) is present. With the range of baselines used, a large effect (of the order 13-50% of central SZ flux density) also comes from primary anisotropies in the CMB. The statistics of these contaminating signals are used to estimate the uncertainty in the SZEs of our cluster sample. D_A^{ps} (Table 4 and 5) is then derived from point source flux corrected ΔI_0 values including uncertainties from remaining point sources and CMB contamination.

6. Instrument and Frequency Comparison

Having adopted the X-ray cluster shape parameters β and θ_c from Reese et al. (2002) and Bonamente et al. (2006) for 4 of our clusters, we can now compare the BIMA/OVRO and AMiBA SZE normalizations. The SZE decrement ΔT is proportional to the integrated pressure along the line of sight as

$$\Delta T = f(x, T_e)\, T_{CMB} \int \sigma_T n_e \frac{kT_e}{m_e c^2} dl. \tag{8}$$

For a standard cluster with a unique temperature and density profile, ΔT would be redshift independent and constant for a fixed observing frequency ν. For a real cluster, variations in ΔT over redshift (at the same observing frequency ν) are then attributed to differences in the cluster ICM physics. If the same cluster, modeled with the same shape parameters, is observed at different frequencies, the difference in the measured values for ΔT depends only on the observing frequencies.

Further, adopting identical X-ray cluster shape parameters, the ratio $\Delta T_0/f(x, T_e)$ ($f(x, T_e) \approx -1.88$ for BIMA/OVRO and $f(x, T_e) \approx -1.46$ for AMiBA) should be frequency independent for any cluster at any redshift. Slight changes in $f(x, T_e)$ from temperature dependent relativistic corrections are taken into account. Fig.3 displays this ratio as a function of redshift for the two cluster models for the AMiBA and BIMA/OVRO observations. For the two lower redshifts the ratios agree to within 10% or better, at higher redshift the discrepancy grows but is still within a factor of two. Both the isothermal β-model and the 100 kpc cut model show the same tendencies here. We stress that choosing the same X-ray shape parameters does not automatically guarantee this consistency, as it is apparently not the case for A1995. Although we adopt the shape parameters from a joint fit from

BIMA/OVRO+*ROSAT* and BIMA/OVRO+*Chandra*, the SZE normalization is derived from AMiBA at 94 GHz only. In order to find a consistent normalization, a proper treatment of foreground, CMB and radio point source contamination (Liu et al. 2009), data analysis and flagging (Wu et al. 2009) is paramount. A1995, which is a possible merger, shows the largest discrepancy in this instrument comparison.

The scaling factor, s_{AB}, between the AMiBA and BIMA/OVRO results ($\Delta T_0/f(x,T_e)_{AMiBA}$ and $\Delta T_0/f(x,T_e)_{BIMA/OVRO}$) for the four clusters is $s_{AB} = 1.27 \pm 0.14$ and $s_{AB} = 1.00 \pm 0.11$ for the 100 kpc cut and the isothermal β-model. This comparison assumes that the center frequencies, 30 GHz for BIMA/OVRO and 94 GHz for AMiBA, represent the weighted bandpass response frequency. For AMiBA this is verified with a bandpass shape measurement showing an approximately symmetric system response (Lin et al. 2009): the SZE spectral function is close to linear over the $86 - 102$ GHz range.

7. Discussion and Conclusion

Our observational error budget is dominated by the uncertainties in the central SZE decrement and X-ray temperature. The central SZE error is large because of CMB primordial noise and lack of angular dynamic range with the current AMiBA configuration, and some uncertainties in the calibration of the instrument.

Our initial cluster sample is selected on SZE strength. Therefore, high-mass clusters, mergers and clusters oriented along the line of sight are included and introduce a complex bias. Single model corrections equally applied to the entire sample tend not to cause significant changes in the estimated H_0. The asphericity correction leads to a $\sim 10\%$ larger value for both the 100 kpc cut and the isothermal β-model because of the systematically larger core radii from the elliptical β-model fits. The point source correction again introduces only a $\sim$ 10-20% change in H_0 for both models, and it is therefore unlikely to be a major cause of H_0 being lower than its current accepted value in the concordance model. Also polytropic temperature corrections for the isothermal β-model, especially for $\gamma > 1$, do not improve the overall sample estimate. The correction appears to be too rough. Slight deviations from $\gamma \equiv 1$ might be meaningful, but need to be better motivated by high-resolution temperature profiles for individual clusters. Fig.2 illustrates that for an individual cluster, one correction or a combination of corrections can bring D_A closely to the value expected from the consensus H_0. This is the case except for A2142, which is an obvious merger with a complicated bimodal structure, probably having boosted ΔT_0, and for A1995. Due to its smaller angular size, A1995 ($z = 0.322$) remains unresolved, so that we have no information on the reason for its large apparent D_A. No apparent point sources have been detected in this cluster. An angular diameter distance roughly in agreement with the expected value (∼1200 Mpc) has been measured at lower frequency in Reese et al. (2002) and Bonamente et al. (2006). The AMiBA 94 GHz observation gives a value about 3 times larger when using the isothermal β-model and even more than 4 times larger when adopting the 100 kpc model.

Having adopted the 100 kpc cut model in order to address the cooling flow and non-isothermality bias, we specifically compare our cooling flow subsample (A1689, A2142, A2261, A2390). Interestingly, the two models yield similar values, $H_0 = 78 \pm 22\,\mathrm{km\,s^{-1}\,Mpc^{-1}}$ and $H_0 = 84 \pm 12\,\mathrm{km\,s^{-1}\,Mpc^{-1}}$ for the isothermal β and the 100 kpc cut model, respectively. All the errors being quoted here are statistical only. Although our sample size is small, we do not find an indication that the 100 kpc cut model significantly improves the estimate. This is in agreement with Bonamente et al. (2006) where a larger cluster sample measured around 30 GHz has shown only a small spread (~ 3 km s^{-1} Mpc^{-1}) in H_0 between the two models. The close agreement between the two models in our sample becomes also apparent when A1995 is excluded from the sample (leaving A1689, A2163, A2261, A2390 for the 100 kpc cut model, and A1689, A2142, A2163, A2261, A2390 for the isothermal β-model): this leads to $H_0 = 79 \pm 9\ \mathrm{km\,s^{-1}\,Mpc^{-1}}$ and $H_0 = 73 \pm 13\ \mathrm{km\,s^{-1}\,Mpc^{-1}}$ for the 100 kpc cut and the isothermal β-model, respectively. When the sample is reduced to include only the two relaxed clusters (A1689, A2390) both models give values very close to the current consensus value of H_0: $H_0 = 76 \pm 7\ \mathrm{km\,s^{-1}\,Mpc^{-1}}$ and $H_0 = 78 \pm 29\ \mathrm{km\,s^{-1}\,Mpc^{-1}}$ for the 100 kpc cut and the isothermal β-model. From this discussion we conclude that the corrections applied to the entire sample are rather unimportant, and likely to be not useful unless motivated by the specific properties of each cluster and determined by a careful and individual analysis. Having a sample free of outliers (A1995 in our case) is paramount. The choice of the detailed cluster model then seems to be less important. A larger sample would naturally further support this. Similar numbers and error bars, based on an isothermal β-model only, have been derived from a five cluster sample in Jones et al. (2005). Aiming at eliminating the cluster orientation bias in an X-ray limited sample above the RASS brightness limit, they find $H_0 = 66^{+11+9}_{-10-8}$ km s^{-1} Mpc^{-1} with a scatter ranging from $H_0 = 34^{+15}_{-10}\,\mathrm{km\,s^{-1}\,Mpc^{-1}}$ to $H_0 = 129^{+60}_{-38}\,\mathrm{km\,s^{-1}\,Mpc^{-1}}$. The authors suggest that large variations in the internal gas kinematics (from mergers) possibly explain this scatter,

Comparing the AMiBA 94 GHz sample with the 30 GHz BIMA/OVRO shows a good agreement between the frequencies with a scaling factor between 1 and 1.27 depending on the cluster model. The cluster causing the single most discrepancy is again A1995. Projecting ahead, we expect that AMiBA in its 13 element expansion will be able to measure 30-50 clusters per year, which will then set more stringent limits to H_0.

Since clumpiness (density inhomogeneities) is not well constrained, we have not attempted to correct for clumping. Excellent X-ray spectroscopy is required to assess the importance of this effect. Detailed observations constraining temperature profiles together with more complicated modeling (especially for mergers) could further reduce systematic errors. This will be addressed in a later paper. Such improvements will also be helpful when the SZE spectra of clusters are studied by combining data from instruments with a variety of angular resolutions and frequencies.

Capital and operational funding for AMiBA came from the Ministry of Education, the National Science Council as part of the Cosmology and Particle Astrophysics (CosPA) initiative and the Academia Sinica. Support from the STFC for MB and KL is also acknowledged.

REFERENCES

Allen, S.W., 1998, MNRAS, 296, 392

Allen, S.W., 2000, MNRAS, 315, 269

Allen, S.W., Ettori, S., Fabian, A.C., 2001, MNRAS, 324, 877

Allen, S.W., Schmidt, R.W., Fabian, A.C., Ebeling, H., 2003, MNRAS, 342, 287

Andersson, K.E., Madejski, G.M., 2004, ApJ, 607, 190

Arnaud, M., Hughes, J.P., Forman, W., Jones, C., Lachieze-Rey, M., Yamashita, K., & Hatsukade, I., 1992, ApJ, 390, 345

Augusto, P., Wilkinson, P.N., Browne, I.W.A., 1998, MNRAS, 324, 877

Augusto, P., Edge, A.C., Chandler, C.J., 2006, MNRAS, 367, 366

Baldi, A., Ettori, S., Mazzotta, P., Tozzi, P., Borgani, S., 2007, ApJ, 666, 835

Battistelli, E.S., De Petris, M., Lamagna, L., Melchiorri, F., Palladino, E., Savini, G., Cooray, A., Melchiorri, A., Rephaeli, Y., Shimon, M., 2002, ApJ, 580, L101

Bauer, F. E., Fabian, A. C., Sanders, J. S., Allen, S. W., Johnstone, R. M., 2005, MNRAS, 359, 1481

Benson, B.A., Church, S.E., Ade, P.A.R., Bock, J.J., Ganga, K.M., Hinderks, J.R., Mauskopf, P.D., Philhour, B., Runyan, M.C., Thompson, K.L., 2003, ApJ, 592, 674

Benson, B.A., Ade, P.A.R., Bock, J.J., Ganga, K.M., Henson, C.N., Thompson, K.L., Church, S.E., 2004, ApJ, 617, 829

Birkinshaw, M., 1979, MNRAS, 187, 847

Birkinshaw, M., Hughes, J.P., Arnaud, K.A., 1991, ApJ, 379, 466

Birkinshaw, M., Hughes, J.P., 1994, ApJ, 420, 33

Birkinshaw, M., 1999, Phys.Rep., 310, 97

Bonamente, M., Joy, M.K., LaRoque, S.J., Carlstrom, J.E., Reese, E.D., Dawson, K.S., ApJ, 2006, 647, 25

Böhringer, H., Tanaka, Y., Mushotzky, R.F., Ikebe, Y., Hattori, M., 1998, A&A, 334, 789

Briel, U.G., Henry, J.P., 1993, A&A, 278, 379

Broadhurst, T., Takada, M., Umetsu, K., Kong, X., Arimoto, N., Chiba, M., Futamase, T., 2005, ApJ, 619L, 143B

Carlstrom, J.E., Joy, M.K., & Grego, L., 1996, ApJ, 456, L75

Carlstrom, J.E., Joy, M.K., Grego, L., Holder, G.P., Holzapfel, W.L., Mohr, J.J., Patel, S., & Reese, E.D., 2000, Phys. Scr., T85, 148

Carroll, S.M., Press, W.H., & Turner, E.L., 1992, ARA&A, 30, 499

Cavaliere, A., & Fusco-Femiano, R., 1976, A&A, 49, 137

Cavaliere, A., Danese, L., de Zotti, G., 1977, ApJ, 217, 6

Challinor, A., & Lasenby, A., 1998, ApJ, 499,1

Chapman, S.C., Scott, D., Borys, C., Fahlman, G.G., 2002, MNRAS, 330, 92

Chen, M.-T., et al., 2009, ApJ, accepted, arXiv:0902.3636

Colafrancesco, S., Marchegiani, P., Palladino, E., 2003, A&A, 397, 27

Colberg, J.M., 2000, MNRAS, 313, 229

Corless, V.L., King, L.J., Clowe, D., 2009, MNRAS, 393, 1235

Cooray, A.R., Grego, L., Holzapfel, W.L., Joy, M., Carlstrom, J.E., 1998, AJ, 115, 1388

Crawford, C. S., Edge, A. C., Fabian, A. C., Allen, S. W., Bohringer, H., Ebeling, H., McMahon, R. G., Voges, W., 1995, MNRAS, 274, 75

Dahle, H., Kaiser, N., Irgens, R.J., Lilje, P.B., Maddox, S.J., 2002, ApJS, 139, 313

De Filippis, E., Sereno, M., Bautz, M.W., & Longo, G., 2005, ApJ, 625, 108

Désert, F.X., et al. 1998, New Astronomy, 3, 655

Dobbs, M., et al., 2006, New Astron. Rev. 50, 960

Duffy, A.R., Schaye, J., Kay, S.T., Dalla Vecchia, C., 2008, MNRAS, 390L, 64

Ebeling, H., Edge, A.C., Allen, S.W., Crawford, C.S., Fabian, A.C., Huchra, J.P., 2000, MNRAS, 318, 333

Ebeling, H., Edge, A. C., Böhringer, H., Allen, S. W., Crawford, C. S., Fabian, A. C., Voges, W., Huchra, J. P., 1998, MNRAS, 301, 881

Ettori, S., Fabian, A.C., 2000, MNRAS, 317, L57

Feretti, L., Fusco-Femiano, R., Giovannini, G., Govoni, F., 2001, A&A, 373, 106

Feretti, L., Orrú, E., Brunetti, G., Giovannini, G., Kassim, N., Setti, G., 2004, A&A, 423, 111

Freedman, W., et al., 2001, ApJ, 553, 47

Girardi, M., Fadda, D., Escalera, E., Giuricin, G., Mardirossian, F., Mezzetti, M., 1997, ApJ, 490, 56

Govoni, F., Markevitch, M., Vikhlinin, A., VanSpeybroeck, L., Feretti, L., Giovannini, G., 2004, ApJ, 605, 695

Grego, L., et al., 2000, ApJ, 539, 39

Grego, L., et al., 2001, ApJ, 552, 2

Gregory, P.C., Condon, J.J., 1991, ApJS, 77, 1011

Grainge, K., Jones, M., Pooley, G., Saunders, R., & Edge, A., 1993, MNRAS, 265, L57

Grainge, K., et al., 2002, MNRAS, 333, 318

Grainge, K., et al., 2003, MNRAS, 341, L23

Halverson, N.W., et al., arXiv:0807.4208

Henry, J.P., Briel, U.G., 1996, ApJ, 472, 137

Herbig, T., & Birkinshaw, M., 1994, BAAS, 26, 1403

Herbig, T., Lawrence, C.R., Readhead, A.C.S., Gulkis, S., 1995, ApJ, 449, L5

Ho, P.T.P., et al., 2009, ApJ, accepted, arXiv:0810.1871

Holzapfel, W.L., Ade, P.A.R., Church, S.E., Mauskopf, P.D., Rephaeli, Y., Wilbanks, T.M., & Lange, A.E., 1997, ApJ, 481, 35

Holzapfel, W.L., Wilbanks, T.M., Ade, P.A.R., Church,S.E., Fischer, M.L., Mauskopf, P.D., Osgood, D.E. & Lange, A.E., 1997, ApJ, 479, 30

Huang, C.-W., et al., 2009, ApJ, submitted

Hughes, J.P., Birkinshaw, M., 1998, ApJ, 501, 1

Itoh, N., Kohyama, Y., Nozawa, S., 1998, ApJ, 502, 7

Jones, M.E., et al., 1993, Nature, 365, 320

Jones, M.E., et al., 2005, MNRAS, 357, 518

Kawahara, H., Kitayama, T., Sasaki, S., Suto, Y., 2007, astro-ph/0705.3288v1

Koch, P.M., et al., 2006, Proceedings of The European Conference on Antennas and Propagation: EuCAP 2006 (ESA SP-626) ed. H. Lacoste & L. Ouwehand. Published on CDROM., p.668.1.

Koch, P.M., et al., 2009, ApJ, accepted, arXiv:0902.2335

Kneissl, R., Jones, M.E., Saunders, R., Eke, V.R., Lasenby, A.N., Grainge, K., Cotter, G., 2001, MNRAS, 328, 783

Komatsu, E., Kitayama, T., Suto, Y., Hattori, M., Kawabe, R., Matsuo, H., Schindler, S., Yoshikawa, K., 1999, ApJ, 516, L1

Kosowsky, A., 2003, New Astron. Rev. 47, 939

Kosowsky, A., 2006, New Astron. Rev. 50, 969

Lamarre, J.M., et al., 1998, ApJ, 507, L5

Lancaster, K., et al., 2005, MNRAS, 359, 16

LaRoque, S.J., Carlstrom, J.E., Reese, E.D., Holder, G.P., Holzapfel, W.L., Joy, M., Grego, L., 2002, astro-ph/0204134v2

LaRoque, S.J., Bonamente, M., Carlstrom, J.E., Joy, M.K., Nagai, D., Reese, E.D., Dawson, K.S., 2006, ApJ, 652, 917

Lemze, D., Barkana, R., Broadhurst, T.J., Rephaeli, Y., 2008, MNRAS, 386, 1092

Lemze, D., Broadhurst, T.J., Rephaeli, Y., Barkana, R., Umetsu, K., 2009, ApJ, submitted, arXiv:0810.3129

Li, C.-T., et al.2006, in Proc.SPIE, Vol.6275, pp. 487-498, Submillimeter Detectors and Instrumentation for Astronomy III

Limousin, M., et al., 2007, ApJ, 668, 643L

Lin, K.-Y., et al., 2009, ApJ, accepted, arXiv:0902.2437

Liu, G.-C., et al., 2009, ApJ, submitted

Mason, B.S., Myers, S.T., Readhead, A.C.S., 2001, ApJ, 555, L11

Markevitch, M., et al., 2000, ApJ, 541, 542

Markevitch, M., Vikhlinin, A., 2001, ApJ, 563, 95

Maurogordato, S., Cappi, A., Ferrari, C., Benoist, C., Mars, G., Soucail, G., Arnaud, M., Pratt, G.W., Bourdin, H., Sauvageot, J.-L., 2007, astro-ph/0712.2715

Miralda-Escudé, J., Babul, A., 1995, ApJ, 449, 18

Molnar, S.M., Birkinshaw, M., Mushotzky, R.F., 2002, ApJ, 570, 1

Molnar, S.M., et al. 2009, ApJ, in preparation

Mroczkowski, T., et al., 2008, arXiv:0809.5077

Muchovej, S., et al., 2007, ApJ, 663, 708

Mushotzky, R. F.; Scharf, C. A., 1997, ApJ, 482, L13

Myers, S.T., Baker, J.E., Readhead, A.C.S., Leitch, E.M., Herbig, T., 1997, ApJ, 485, 1

Navarro, J.F., Frenk, C.S., White, S.D.M., 1997, ApJ, 490, 493

Nishioka, H., et al., 2009, ApJ, accepted, arXiv:0811.1675

Nord, M., et al., 2009, arXiv:0902.2131v1

Nozawa, S., Itoh, N., Kawana, Y., Kohyama, Y., 2000, ApJ, 536, 31

Oegerle, W.R., Hill, J.M., & Fitchett, M.J., 1995, AJ, 110, 32

Okabe, N., Umetsu, K., 2007, astro-ph/0702649

Padin, S., et al., 2002, PASP, 114, 83

Patel, S.K., et al, 2000, ApJ, 541, 37

Peres, C.B., Fabian, A.C., Edge, A.C., Allen, S.W., Johnstone, R.M., & White, D.A., 1998, MNRAS, 298, 416

Perlmutter, S., Aldering, G., Goldhaber, G., Knop, R., Nugent, P., et al. 1999, ApJ, 519, L115

Pierre, M., Le Borgne, J.F., Soucail, G., Kneib, J.-P., 1996, A&A, 311, 413

Pointecouteau, E., et al., 2001, ApJ, 552, 42

Pratt, G.W., Arnaud, M., Aghanim, N., 2001, in: Proceedings of 'Galaxy Clusters and the High Redshift Universe Observed in X-rays', XXIth Moriond Astrophysics Meeting

Puy, D., Grenacher, L., Jetzer, Ph., Signore, M., 2000, A&A, 363, 415

Reese, E.D., Carlstrom, J.E., Joy, M., Mohr, J., Grego, L., Holzapfel, W.L., 2002, ApJ, 581, 53

Rephaeli, Y., 1995. Annu. Rev. Astron. Astrophys. 33, 541

Rephaeli, Y., Gruber, D., Arieli, Y., 2006, ApJ, 649, 673

Riess, A.G., et al., 2005, ApJ, 627, 579

Rowan-Robinson, M., 1985, *The Cosmological Distance Ladder*, Freeman, New York

Sand, D.J., Treu, T. Ellis, R.S., Smith, G.P., 2005, ApJ, 627, 32S

Sanderson, A.J.R., 2003, Ponman, T.J., 2003, MNRAS, 345, 1241

Schmidt, R.W., Allen, S.W., Fabian, A.C., 2004, MNRAS 352, 1413

Silk, J., White, S.D.M., 1978, ApJ, 226, L103

Spergel, D., 2003, ApJS, 148, 175

Squires, G., Kaiser, N., Babul, A., Fahlmann, G., Woods, D., Neumann, D.M., Böhringer, H., 1996, ApJ, 461, 572

Sunyaev, R.A., Zel'dovich, Ya.B., 1972, Comm. Astrophys. Space Phys. 4, 173

Staniszewski, Z., et al., 2008, arXiv:0810.1578

Udomprasert, P.S., Mason, B.S., Readhead, A.C.S., Pearson, T.J., 2004, ApJ, 615, 63

Umetsu, K., Broadhurst, T.J., 2008, ApJ, 684, 177

Umetsu, K., et al. 2009, ApJ, accepted, arXiv:0810.0969

White, D. A., 2000, MNRAS, 312, 663

White, R.L., Becker, R.H., 1992, ApJS, 79, 331

Wu, J.H.P., et al., 2009, ApJ, accepted, arXiv:0810.1015

Xue, S.-J., Wu, X.-P., 2002, ApJ, 576, 152

Zemcov, M., Borys, C., Halpern, M., Mauskopf, P., Douglas, S., 2007, MNRAS, 376, 1073

Zwart, J.T.L., et al., 2008, arXiv:0807.4208

This preprint was prepared with the AAS LaTeX macros v5.2.

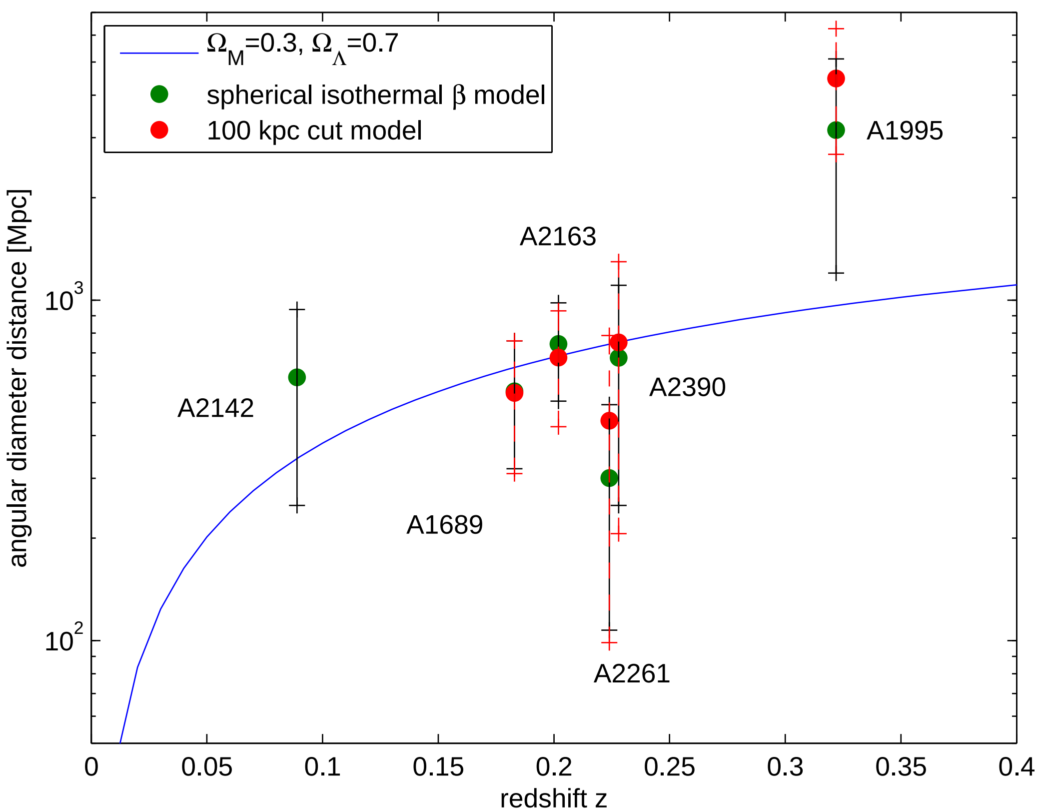

Fig. 1.— Comparison between angular diameter distances derived from a 100 kpc cut model and the spherical isothermal β-model (Tables 2 and 3). Errors are 1σ observational uncertainties. The solid line shows the angular diameter distance function for $\Omega_M = 0.3, \Omega_\Lambda = 0.7$, $H_0 = 70$ km s^{-1} Mpc^{-1}.

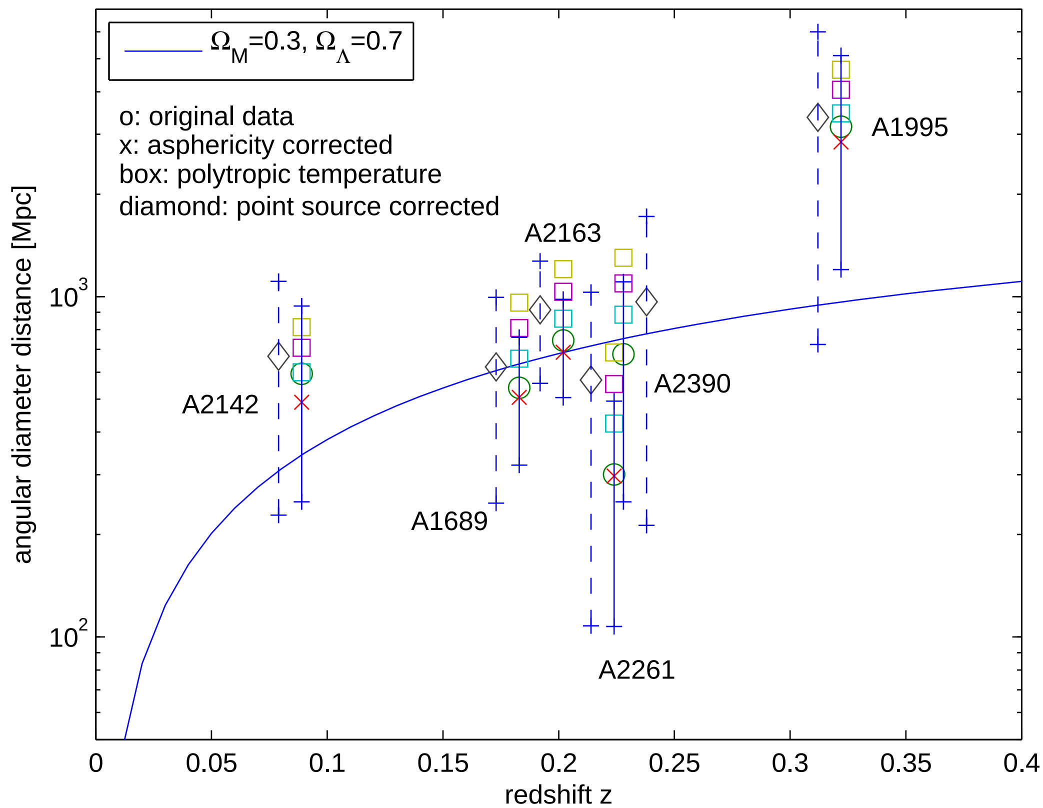

Fig. 2.— Measured angular diameter distances, assuming a spherical isothermal β-model with the values from Table 3. The original uncorrected data ($\circ$) are shown together with model corrections for asphericity ($\times$), non-isothermality ($\Box$) and point sources ($\Diamond$). All corrections are with respect to the original data. For better clarity the point source correction is slightly shifted to the left (to the right for A2390). Errors are 1σ observational uncertainties. Errors for the point source correction additionally include contributions from point sources and CMB. The solid line shows the angular diameter distance function for $\Omega_M = 0.3, \Omega_\Lambda = 0.7$, $H_0 = 70$ km s^{-1} Mpc^{-1}.

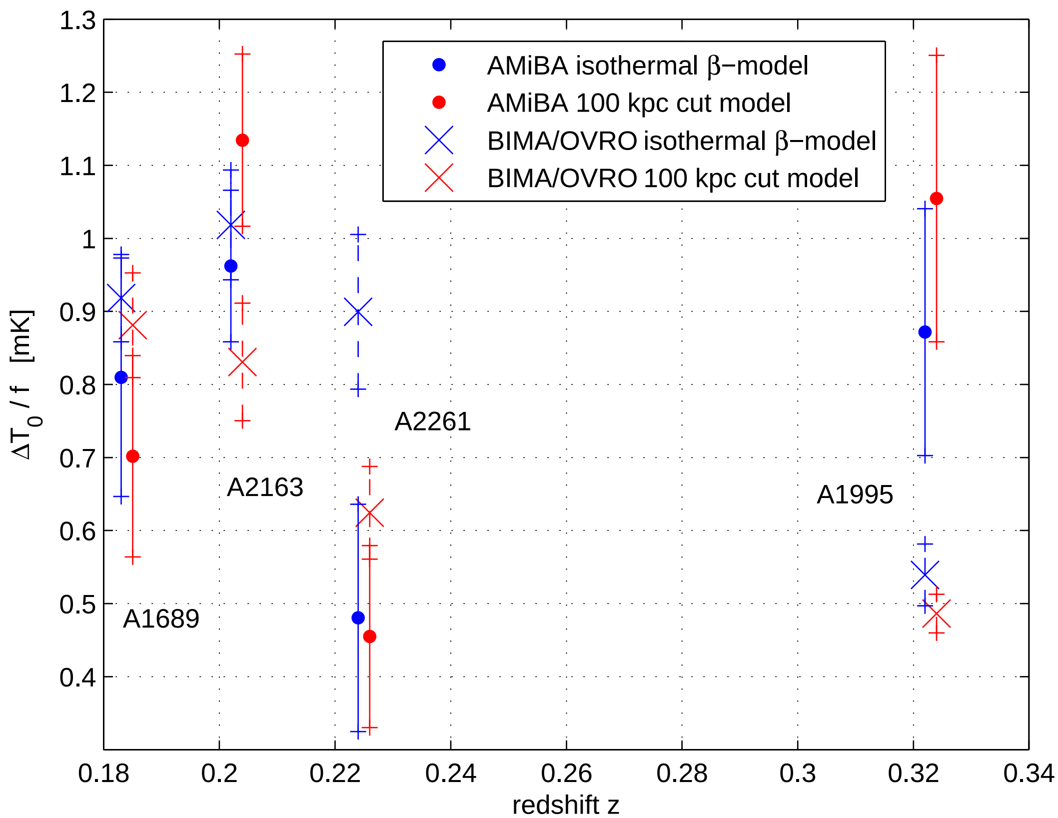

Fig. 3.— AMiBA and BIMA/OVRO comparison of the frequency normalized central SZE normalization $\Delta T_0/f(x,T_e)$ for four clusters where the samples overlap. All values agree to within factor of two and to within 10% for the two lower redshift clusters. Values for BIMA/OVRO are from Reese et al. (2002), Table 7, for the isothermal β-model, and from Bonamente et al. (2006), Table 4, for the 100 kpc cut model.

Table 1. AMiBA Initial Cluster Sample: Basic Properties

Cluster	R.A.	Decl.	$t_{\rm int}$/hr	S/N	beam	size	flux density/mJy	Notes[a]
A1689	$13^{\rm h}11.49^{\rm m}$	$-1^\circ 20.47'$	7.11	6.0	$6.3'$	$(5.7')$	-168	CF, NC, R(?)
A1995	$14^{\rm h}52.84^{\rm m}$	$58^\circ 02.80'$	5.56	6.4	$6.6'$	$(6.8')$	-161	M(?), NC, X
A2142	$15^{\rm h}58.34^{\rm m}$	$27^\circ 13.61'$	5.18	13.7	$6.5'$	$9.0'$	-316	M, CF, NI, NC
A2163	$16^{\rm h}15.57^{\rm m}$	$-6^\circ 07.43'$	6.49	11.7	$6.6'$	$11.2'$	-346	M, NI, NC, RH
A2261	$17^{\rm h}22.46^{\rm m}$	$32^\circ 07.62'$	8.87	5.2	$6.4'$	$(5.8')$	-90	M(?), CF, NI
A2390	$21^{\rm h}53.61^{\rm m}$	$17^\circ 41.71'$	11.02	6.6	$6.4'$	$8.0'$	-158	CF, R

Note. — Properties of the initial AMiBA SZE observations: pointing coordinates in J2000; total on-source integration time after removing bad data; S/N ratio of the cleaned images; FWHM of the azimuthally averaged dirty beam; cluster size (again azimuthally averaged FWHM in the image plane) obtained from the cleaned images; cleaned images peak flux. The brackets indicate that the cluster appears unresolved in the AMiBA SZE image. A detailed description and derivation of these numbers are given in Wu et al. (2009).

[a]Cluster properties summarized from section 3. M: merger; CF: cooling flow; NI: non-isothermal; NC: non-circular isophotes; RH: radio halo; X: X-ray point sources; R: relaxed.

Table 2. Cluster parameters for 100 kpc cut model

Cluster	*Chandra* 0.7 − 7.0 keV							AMiBA SZE[f]	
	z	β	θ_c (arcsec)	S_{X0} [d] (counts cm^{-2} arcmin^{-2})	kT_e (keV)	Λ_{ee} [e] (counts s^{-1} cm^3)	ref	ΔI_0 ($\times 10^5$ Jy/sr)	ΔT_0 (μK)
A1689	0.183	$0.686^{+0.010}_{-0.010}$	$48.0^{+1.5}_{-1.7}$	$36.1^{+1.4}_{-1.3}$	$10.1^{+0.5}_{-0.6}$	2.96×10^{-15}	1	-2.24 ± 0.44	-1030±200
A1995	0.322	$0.923^{+0.021}_{-0.023}$	$50.4^{+1.4}_{-1.5}$	$24.9^{+0.4}_{-0.4}$	$9.1^{+0.5}_{-0.5}$	2.35×10^{-15}	1	-3.39 ± 0.63	-1560±290
A2142[a]	0.089	...	...	...	...	...	...	...	...
A2163[b]	0.202	$0.700^{+0.07}_{-0.07}$	$78.8^{+0.6}_{-0.6}$	$69.2^{+0.7}_{-0.7}$	$13.8^{+0.8}_{-0.7}$	2.52×10^{-15}	1	-3.56 ± 0.37	-1640±170
A2261	0.224	$0.628^{+0.030}_{-0.020}$	$29.2^{+4.8}_{-2.9}$	$14.4^{+2.2}_{-2.3}$	$7.9^{+0.8}_{-1.1}$	2.80×10^{-15}	1	-1.46 ± 0.40	-670±180
A2390[c]	0.228	$0.58^{+0.058}_{-0.058}$	$34.4^{+3.4}_{-3.4}$	$25^{+2.5}_{-2.5}$	$11.5^{+1.5}_{-1.6}$	2.66×10^{-15}	2	-2.42 ± 0.36	-1110±170

[a]excluded from the sample due to its obvious bimodal structure in the high-resolution X-ray image.

[b]β fixed to a fiducial value of 0.7 in Bonamente et al. (2006), a 10% error is assumed.

[c]a 10% error is assumed for S_{X0}, a sample averaged cooling function is adopted.

[d]in order to calculate D_A, the integrated counts need to be further divided by the integration times, Table 1 in Bonamente et al. (2006), which then leads to the dimensionally consistent units (counts s^{-1} cm^{-2} arcmin^{-2}), listed in Table

[e]electron-electron cooling function where the factor μ_H/μ_e (Table 3 is absorbed.

[f]Best-fit values for ΔI_0 without contamination estimation from point sources and CMB (Liu et al. 2009).

References. — (1) Bonamente et al. (2006). (2) Allen et al. (2001)

Table 3. Cluster Parameters for isothermal spherical β-model

Cluster	*ROSAT* 0.5 − 2.0 keV								AMiBA SZE[b]	
	z	β	θ_c (arcsec)	S_{X0} (ergs s^{-1} cm^{-2} $arcmin^{-2}$)	kT_e (keV)	Λ_{eH0} (ergs s^{-1} cm^3)	μ_H/μ_e	ref	ΔI_0 ($\times 10^5$ Jy/sr)	ΔT_0 (μK)
A1689	0.183	$0.609^{+0.005}_{-0.005}$	$26.6^{+0.7}_{-0.7}$	$6.01^{+0.18}_{-0.15} \times 10^{-12}$	$9.66^{+0.22}_{-0.20}$	6.158×10^{-24}	1.20	1	-2.59 ± 0.53	-1190 ± 240
A1995	0.322	$0.770^{+0.117}_{-0.063}$	$38.9^{+6.9}_{-4.3}$	$1.08^{+0.08}_{-0.07} \times 10^{-12}$	$8.59^{+0.86}_{-0.67}$	6.434×10^{-24}	1.20	1	-2.80 ± 0.54	-1290 ± 250
A2142	0.089	$0.740^{+0.010}_{-0.010}$	$188.4^{+13.2}_{-13.2}$	$0.92^{+0.09}_{-0.09} \times 10^{-12}$	$9.70^{+1.50}_{-1.10}$	6.232×10^{-24}	1.20	2,3,4	-1.97 ± 0.20	-910 ± 90
A2163	0.202	$0.674^{+0.011}_{-0.008}$	$87.5^{+2.5}_{-2.0}$	$1.36^{+0.03}_{-0.03} \times 10^{-12}$	$12.2^{+1.1}_{-0.7}$	6.135×10^{-24}	1.20	1	-3.02 ± 0.33	-1390 ± 150
A2261	0.224	$0.516^{+0.014}_{-0.013}$	$15.7^{+1.2}_{-1.1}$	$4.31^{+0.26}_{-0.26} \times 10^{-12}$	$8.82^{+0.37}_{-0.32}$	6.359×10^{-24}	1.20	1	-1.54 ± 0.50	-710 ± 230
A2390[a]	0.228	$0.600^{+0.060}_{-0.060}$	$28.0^{+2.8}_{-2.8}$	$3.45^{+0.35}_{-0.35} \times 10^{-12}$	$10.13^{+1.22}_{-0.99}$	6.238×10^{-24}	1.20	5,6	-2.57 ± 0.41	-1180 ± 190

[a]a 10% error is assumed for $(\beta, \theta_c, S_{X0})$ for which the original reference does not give an error estimate

[b]Best-fit values for ΔI_0 without contamination estimation from point sources and CMB (Liu et al. 2009).

References. — (1) Reese et al. (2002). (2) Henry & Briel (1996). (3) Sanderson & Ponman (2003). (4) Lancaster et al. (2005). (5) Böhringer et al. (1998). (6) Allen (2000).

Table 4. D_A and observational error budget (1σ uncertainties) - 100 kpc cut model

Cluster	100 kpc Cut Model								Model Corrections^f	
	$\mathrm{Fit}^a_{X,\beta}$ (%)	$\mathrm{Fit}^a_{X,\theta_c}$ (%)	$\mathrm{Fit}^a_{X,S_{X0}}$ (%)	Fit^b_X (%)	T^a_e (%)	$\mathrm{Fit}^{a,c}_{SZ}$ (%)	Total^d (%)	D_A (Mpc)	D^{ell}_A (Mpc)	D^{ps}_A (Mpc)
A1689	± 4.0	± 4.8	± 5.3	± 8.2	± 16.1	± 38.0	± 42.1	528 ± 222	495	606 ± 354
A1995	± 4.3	± 4.1	± 2.3	± 6.4	± 16.1	± 36.1	± 40.1	4421 ± 1771	3990	3697 ± 2683
A2142	...	...	...	...	...	...	...	...	...	...
A2163	± 26.6	± 1.1	± 1.4	± 26.7	± 16.0	± 20.6	± 37.3	670 ± 250	619	708 ± 319
A2261	± 12.8	± 22.5	± 28.0	± 39.0	± 42.4	± 52.1	± 77.7	437 ± 340	433	1124 ± 1011
A2390	± 36.3	± 15.0	± 15.1	± 42.7	± 50.8	± 29.3	± 72.6	742 ± 538	...	1088 ± 905

[a]error contribution of each individual fitting parameter

[b]combined in quadrature (X-ray parameters: β, θ_c, S_{X0}), strictly speaking β and θ_c should not be combined in quadrature because they are tightly correlated

[c]does not include uncertainties from radio point sources and CMB contamination, included in D_A^{ps}

[d]combined in quadrature

[e]D_A from non-relativistic derivation

[f]all corrections are with respect to the 100 kpc cut model and ΔI_0 from Table 2; error budget for D_A^{ell} is identical to the budget for D_A, not shown here; D_A^{ps} is derived from point source corrected ΔI_0 values and includes uncertainties from radio point sources and CMB contamination

Table 5. D_A and observational error budget (1σ uncertainties) - isothermal spherical β-model

Cluster	Isothermal Spherical β-Model								Model Corrections[e]		
	$\mathrm{Fit}^a_{X,\beta}$ (%)	$\mathrm{Fit}^a_{X,\theta_c}$ (%)	$\mathrm{Fit}^a_{X,S_{X0}}$ (%)	Fit^b_X (%)	T^a_e (%)	$\mathrm{Fit}^{a,c}_{SZ}$ (%)	Total[d] (%)	D_A (Mpc)	D^{ell}_A (Mpc)	D^T_A (Mpc)	D^{ps}_A (Mpc)
A1689	±2.7	±3.8	±3.9	±6.1	±6.2	±39.8	±40.7	539 ± 220	506	[658, 960][f]	622 ± 374
A1995	±28.8	±25.3	±10.1	±40.5	±28.0	±37.6	±61.9	3156 ± 1955	2849	[3457, 4642]	3362 ± 2639
A2142	±3.2	±10.2	±14.9	±18.3	±51.1	±20.2	±58.0	594 ± 344	490	[599, 814]	668 ± 440
A2163	±3.9	±3.7	±3.1	±6.2	±22.8	±21.6	±32.0	743 ± 238	687	[861, 1204]	915 ± 358
A2261	±12.9	±10.7	±8.7	±18.9	±11.4	±60.3	±64.2	300 ± 193	297	[424, 685]	569 ± 461
A2390	±34.1	±15.2	±15.3	±41.1	±36.3	±31.3	±63.1	677 ± 428	···	[885, 1301]	967 ± 754

[a]error contribution of each individual fitting parameter

[b]combined in quadrature (X-ray parameters: β, θ_c, S_{X0}), strictly speaking β and θ_c should not be combined in quadrature because they are tightly correlated

[c]does not include uncertainties from radio point sources and CMB contamination, included in D_A^{ps}

[d]combined in quadrature

[e]all corrections are with respect to the isothermal spherical β model and ΔI_0 from Table 3; error budget for D_A^{ell} and D_A^T is identical to isothermal spherical β-model (D_A), not shown here; D_A^{ps} is derived from point source corrected ΔI_0 values and includes uncertainties from radio point sources and CMB contamination

[f]interval corresponding to polytropic temperature index $\gamma \in [1.1, 1.3]$

Table 6. H_0 for Different Models and Corrections ($\Omega_M = 0.3, \Omega_\Lambda = 0.7$)

Cluster Model	full sample	CF[a]	R[b]
isothermal β-model			
Original data	50 ± 16	78 ± 22	78 ± 29
Asphericity corrected	54 ± 16	84 ± 21	81 ± 6
Polytropic temperature: $\gamma = 1.1$	43 ± 12	65 ± 15	62 ± 5
Polytropic temperature: $\gamma = 1.2$	36 ± 9	53 ± 11	51 ± 4
Polytropic temperature: $\gamma = 1.3$	31 ± 7	44 ± 8	43 ± 3
Point source corrected	42 ± 10	59 ± 11	61 ± 9
100 kpc cut model			
Original data	34±15	84 ± 12	76 ± 7
Asphericity corrected	37 ± 11	56 ± 10	61 ± 15
Point source corrected	38 ± 11	54 ± 8	58 ± 13

[a]only cooling flow clusters: A1689, A2142, A2261, A2390

[b]only relaxed clusters: A1689, A2390

Table 7. H_0 systematic errors (%) from cluster sample

Systematic	Effect (%)
Density inhomogeneities	-30
Non-isothermality	$+(10-20)$ / 0
Asphericity[a]	$\pm(8-15)$ / $\pm(9-15)$
Kinetic SZE[a]	±2.5 / ±3
CMB[a]	±20 / ±21
Undetected radio point sources[b]	±16 / ±20
AMiBA absolute calibration	±10
X-ray calibration[c]	±10 / ±5
Total[d]	${}^{+35}_{-44}$ / ${}^{+33}_{-45}$

Note. — If not indicated else, errors apply both to the isothermal β and the 100 kpc cut model. Otherwise values are listed for the 100 kpc cut model, followed by those for the isothermal β-model, essentially differing in the sample variance factor, $1/\sqrt{5}$ or $1/\sqrt{6}$, or the sample average.

[a]Including sample variance factor

[b]Sample average

[c]from Reese et al. (2002) and Bonamente et al. (2006)

[d]Combined in quadrature